

# **The Influence of Zinc Electrode Substrate, Electrolyte Flow Rate and Current Density on Zinc-Nickel Flow Cell Performance**

David P. Trudgeon<sup>a</sup>, Adeline Loh<sup>a</sup>, Habib Ullah<sup>a</sup>, Xiaohong Li<sup>a\*</sup>

<sup>a</sup> Renewable Energy Group, College of Engineering, Mathematics and Physical Sciences, University of Exeter, Penryn Campus, Cornwall TR10 9FE, UK

Vladimir Yufit<sup>b</sup>, Nigel Brandon<sup>b</sup>

<sup>b</sup> Department of Earth Science & Engineering, Imperial College London SW7 2AZ, UK

Maocheng Liu<sup>c</sup>, Lingbin Kong<sup>c</sup>

<sup>c</sup> State Key Laboratory of Advanced Processing and Recycling of Non-ferrous Metals, School of Materials Science and Engineering, Lanzhou University of Technology, Lanzhou 730050, China

\* Corresponding author: Xiaohong Li ([X.Li@exeter.ac.uk](mailto:X.Li@exeter.ac.uk))

## **Abstract**

This work aims to identify a suitable material for use as a zinc electrode substrate material in alkaline media, then employ this to study the effect of electrolyte flow rate and current density on zinc-nickel flow cell performance. Three metallic and four graphite composite materials are investigated, with the coulombic efficiency of zinc electrode charge / discharge cycling found to increase as hydrogen evolution onset potentials become more negative. A graphite / PVDF composite substrate demonstrates the highest coulombic efficiency at 96.7 % and the most negative hydrogen evolution onset potential at -1.595 V vs. Hg/HgO. Using this material, the effect of electrolyte flow rate and current density on a zinc-nickel flow cell is investigated. Zinc morphology and flow cell performance is related to the ratio of applied current density to limiting current density. At values between 0.47 and 1, boulder type zinc morphologies have been shown to occur, with smooth and compact zinc deposits resulting from current density ratios of 0.39 and below. Stable zinc-nickel flow cell performance is achieved over 200 cycles with coulombic, voltaic and energy efficiencies of 98.3, 88.1 and 86.6 % respectively, at a current density of 20 mA cm<sup>-2</sup>.

**Keywords:** Electrolyte additive; Redox flow battery; Zinc electrode; Zinc electrodeposition;

## 1. Introduction

Redox flow batteries (RFBs) are seen as a promising energy storage technology for grid-scale applications, possessing advantages such as flexibility, long lifetime, fast response, safe operation, independence of geographical factors, potentially enabling the integration of intermittent but growing fast renewable energy sources into power grids [1]. Within the RFB family, the zinc–nickel redox flow battery (Zn–Ni RFB) has attracted research attention from the beginning of the 21<sup>st</sup> century due to (i) the rapid kinetics of its redox couples allowing both charging and discharging with minimal overpotentials, (ii) a high theoretical cell potential of 1.73 V leading to enhanced power density, (iii) cost-competitiveness and environmentally benign nature and, (iv) capability for membrane free operation, reducing the cost and design complexity of the battery significantly. So far, published results have largely been restricted to small flow cells but the results are promising. It has been reported in several studies [2–6] that Zn–Ni RFB systems in general display cell voltages  $> 1.6$  V on discharge, coulombic efficiencies  $> 95\%$ , and energy efficiencies over 80%. There are, however, challenges associated with the Zn–Ni RFB system. Zinc morphology and the parasitic hydrogen evolution reaction (HER) at the negative electrode must need to be controlled, and the amount of the active material at the positive electrode needs to be increased in order to improve capacity and develop a durable and efficient system.

Zn–Ni RFB performance is affected by complex interactions between a number of operational parameters including electrolyte composition, additives to the electrolyte, pH, temperature, electrode substrate material, operating current density, cell geometry, and electrolyte flow rate, etc. For example, the influence of electrolyte composition has been studied previously [7–10]. It was found that zinc morphology improves with increasing zincate content while the parasitic HER is suppressed [8,9]. We have recently

reported that high concentrations of KOH inhibit zinc reduction by limiting the transport of  $Zn^{2+}$  to the electrode, while nickel electrode overpotentials are found to be reduced with increasing KOH concentrations due to the availability of  $OH^-$  for the nickel oxidation reaction [11]. For electrolyte additives, substantial research efforts have been made on the use of metals and their oxides/hydroxides as additives (e.g. Hg, Pb, Bi, Sn) [11–15] as well as organic additives such as polyvinyl alcohol (PVA), polyethylenimine (PEI), polyethylene glycol (PEG) [11,16–20] and quaternary alkyl ammonium (QAA) salts [11,21–26]. The benefits and drawbacks of these additives have been reported in detail [11,22,24]. Cheng *et al.* reported the effect of electrolyte temperature on Zn-Ni RFB performance, finding that the system can operate between 273 K and 313 K [27] and both coulombic and energy efficiencies improve with temperature, from 81 % and 53 % at 273 K to 96 % and 79 % at 313 K respectively.

In this paper, we examine the effect of zinc electrode substrate material, electrolyte flow rate, and current density on Zn-Ni RFB performance. It has been shown that zinc electrode substrate material influences both zinc morphology and hydrogen evolution [3,28,29]. Metallic substrates are commonly studied including silver, cadmium, bismuth, copper, tin and nickel. Compact zinc morphologies and high hydrogen evolution overpotentials have been reported using tin, copper, bismuth and cadmium substrates [3,29–31] while nickel substrates have been shown to produce porous zinc morphologies due to significant hydrogen evolution [29]. The alloying of zinc with metallic substrates has also been reported in the cases of copper [3,29,31,32], gold [31] and thallium [33], which can modify hydrogen evolution overpotentials and coulombic efficiency after extended cycling. While carbon-based materials have been widely used in RFB technologies [1], previous research into these as zinc electrode substrates in alkaline systems is relatively sparse. The use of carbon and carbon composite materials in the acidic zinc-cerium and zinc-bromine RFB systems has been

studied by Nikiforidis *et al.*, with graphite composite materials containing polyvinylidene fluoride (PVDF) and polyvinyl ester (PVE) demonstrating mechanical stability over extended cycling, and coulombic efficiencies in excess of 95 % [34,35].

Electrolyte flow rate is a significant factor in controlling zinc morphology due to its influence on the mass transport of zincate [36–38]. Previous work has demonstrated that increasing electrolyte flow rates improve zinc morphology by enhancing mass transport of zincate, thus facilitating charge transfer limited zinc reduction [36,39]. Hydrogen evolution is also inhibited by maintaining the concentration of zincate at the electrode surface by forced convection, as reported by Ito *et al.* [40].

The influence of current density on the morphology of zinc has been studied by several researchers [8,9,36,41]. The quality of zinc deposition is reported to deteriorate with increasing current density due to higher mass transport requirements, resulting in diffusion controlled zinc reduction. For example, Cheng *et al.* applied current densities up to 300 mA cm<sup>-2</sup> to a zinc-nickel flow cell, reporting compact zinc depositions at 40 mA cm<sup>-2</sup>, transitioning to dendritic morphologies at 300 mA cm<sup>-2</sup> [41]. The resultant energy efficiencies demonstrated significant deterioration, from 82.6 % at 40 mA cm<sup>-2</sup> to 50.7 % at 300 mA cm<sup>-2</sup>.

Specifically in this research, three metallic electrode substrate materials (copper, tin, and nickel) [2,6,29,42] and four graphite / polymer composite materials are selected and investigated in terms of their effect on hydrogen evolution and coulombic efficiency at the zinc electrode. Though there are some studies reporting these substrate materials for zinc electrode but often in the static battery system, the published papers on the effect of substrate materials on zinc electrode in flowing electrolyte environments has been rare. Then based on experimental data, the best performing substrate is utilised in a zinc-nickel flow cell under varying electrolyte flow rates and current densities,

employing our preceding findings on electrolyte composition and concentration [11,43], with an aim of demonstrating stable and highly efficient operation of Zn-Ni RFB system.

## 2. Experimental

### 2.1 Electrolyte chemicals

The base electrolyte used for cyclic voltammetry (CV), chronoamperometry, chronopotentiometry and galvanostatic flow cell cycling is a 6 M KOH (Acros Organics, analytical grade, 85 %) and 0.5 M ZnO (Fisher Chemical, AR grade, 99.5+ %) solution. Tetraethylammonium hydroxide (TEAH, Sigma-Aldrich, 20 % wt. in H<sub>2</sub>O) is utilised as an electrolyte additive where stated. For linear sweep voltammetry (LSV), a 6 M KOH solution is employed with no addition of ZnO in order to examine the effect of substrate materials on hydrogen evolution. All chemicals are used as received.

### 2.2 Electrode materials and preparation

The zinc electrode substrate materials under investigation are listed in *Table 1*. For use in the zinc-half cell, the materials are cut into segments of 1.5 cm × 5 cm, washed with deionised water, then masked to expose an area of 0.25 cm<sup>2</sup> (0.5 cm × 0.5 cm) using polypropylene tape with acrylic adhesive (Avon tapes, AVN9811060K, 25 μm thickness) before a final rinse prior to use. The Hg/HgO reference electrode is prepared in a 6 M KOH solution using the following chemicals; mercury (Acros Organics, 99.999 % metals basis) and mercury (II) oxide (Acros Organics, 99+ %). The counter electrode is platinum mesh (Alfa Aesar, 99.9 % metals basis, 0.1 mm dia. wire, 52 mesh) of 2 cm<sup>2</sup> area (1 cm × 2 cm). Zinc–nickel flow cell cycling is conducted using

the BMA5 graphite / PVDF composite as the zinc electrode substrate material, cut into 2 cm × 2 cm pieces, polished as above and washed with de-ionised water, then masked to expose an area of 1 cm<sup>2</sup> (1 cm × 1 cm) using polypropylene tape with acrylic adhesive before use. The nickel electrode consists of a commercial sintered nickel (Jiansu Highstar Battery Manufacturing Co. Ltd.) cut into 2 cm × 2 cm sections then masked to expose an area of 1 cm<sup>2</sup> (1 cm × 1 cm) using polypropylene tape with acrylic adhesive before use. An Hg/HgO reference electrode is utilised in 6 M KOH.

### 2.3 Electrochemical methods

All electrochemical measurements are taken at room temperature (293 K) using a BioLogic SP-300 potentiostat and EC-Lab software. CV, LSV and zinc half-cell cycling tests are carried out in a 20 mL glass cell using a three-electrode half-cell configuration. CV is conducted at 10 mV s<sup>-1</sup> across the potential range of -0.8 to -1.6 V vs. Hg/HgO. LSV is conducted at 1 mV s<sup>-1</sup> from -1.0 V vs. Hg/HgO until the cathodic hydrogen evolution current density reaches 100 mA cm<sup>-2</sup>.

Zinc half-cell cycling tests are carried out over 10 cycles using chronopotentiometry to facilitate zinc reduction at -20 mA cm<sup>-2</sup> for 30 minutes and zinc oxidation at 20 mA cm<sup>-2</sup> to a cut-off potential of -1.0 V vs. Hg/HgO. For these experiments, the electrolyte is stirred at 600 rpm throughout to minimise diffusion limitations, using a Camlab MS-H280-Pro magnetic stirrer and a PTFE stir bar.

Full zinc-nickel flow cell cycling tests are conducted using a C-Flow laboratory cell (C-Tech Innovation, 1 cm × 1 cm electrode area, 1.2 cm electrode gap). A peristaltic pump (Watson-Marlow 323S) and Marprene tubing (Watson Marlow, 3.2 mm I.D., 6.4 mm O.D.) are employed to pump 100 mL of the electrolyte solution containing 6 M KOH + 0.5 M ZnO, with or without 15 mM TEAH additive, through the cell. Volumetric flow

rates of 70 to 840 ml min<sup>-1</sup> are employed, providing average linear velocities between 1 and 12 cm s<sup>-1</sup>. Galvanostatic cycling tests are carried out at charge current densities between 20 and 80 mA cm<sup>-2</sup> to a capacity of 3 mA h and discharged at the same current density to a cut-off cell potential of 0.8 V. Electrodepositions of zinc are obtained from the flow cell at the end of galvanostatic cycling tests by applying a final charge phase to 3 mA h capacity.

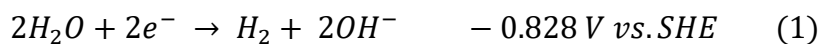
The surface morphology of the samples is characterised with an FEI Quanta FEG 650 SEM, operated at an accelerating voltage of 5 kV and a working distance of 5 mm. A Bruker D8 Advance X-ray Diffractometer with Cu tube source ( $\lambda = 1.5418 \text{ \AA}$ ) and Bruker Diffraction Suite EVA software is employed for XRD. The kinematic viscosity of the electrolyte is measured utilising an SI analytics 516 13 micro-Ostwald viscometer, with five measurements made at 293 K and the average taken. Measurement error is found to be within +/- 2%.

### **3. Results and discussion**

#### **3.1 Effect of zinc electrode substrate material**

##### **3.1.1 Hydrogen evolution reaction**

During zinc reduction in alkaline media, hydrogen evolution can take place as a competing reaction via reaction (1) below [9,44]. This parasitic HER attenuates the coulombic efficiency of the zinc electrode and can cause porosity in the deposited zinc. The activity of the electrode substrate material for HER can therefore influence the performance of the zinc electrode.



Here, the effect of substrate material on hydrogen evolution onset potentials has been assessed by linear sweep voltammetry in 6 M KOH electrolyte with no ZnO. As such, any observed cathodic current response can be attributed to hydrogen evolution. The resultant HER polarisation curves and Tafel slopes are given in **Fig. 1**, with the HER onset potentials ( $E_{HER}$ ) displayed in **Table 2**. As shown in **Fig. 1**, the influence of metallic substrate materials on HER potentials is significant, and can be attributed to the relative hydrogen binding energies of the substrate material. Reaction (1) involves the formation and cleavage of M-H bonds, with intermediate bond strengths resulting in the highest HER activity. If the binding energy is weak, the formation of M-H bonds will be insufficient to facilitate significant HER, whereas for strong binding energies the cleavage of M-H bonds will be retarded [45,46].

Of the materials studied here, nickel demonstrates the highest HER activity, with an HER onset potential,  $E_{HER}$  of -1.126 V vs. Hg/HgO (**Fig. 1a**) and a Tafel slope of 154 mV dec<sup>-1</sup> (**Fig. 1c**), this being in close agreement with previously reported values of 160 mV dec<sup>-1</sup> on polycrystalline nickel under similar conditions [47]. In alkaline media nickel has been shown to possess hydrogen binding energies favourable to HER [45] and significant research efforts have focused on nickel based alkaline HER catalysts [48]. **Fig. 1a** displays an  $E_{HER}$  206 mV more negative on copper than on nickel, at -1.332 V vs. Hg/HgO, and a Tafel slope of 190 mV dec<sup>-1</sup> (**Fig. 1c**). This is lower than the value of 226 mV dec<sup>-1</sup> reported by Sheng *et al.*, in that case however, an electrolyte containing 0.1 M KOH was employed [45]. Copper has been shown to have weaker hydrogen binding energies than nickel [45,49,50], and the reduction of HER activity compared to nickel can therefore be attributed to reduced proton adsorption at the substrate. The hydrogen bond strength on tin is further reduced [46], resulting in a much higher Tafel slope of 252 mV dec<sup>-1</sup> and  $E_{HER}$  values 245 mV and 451 mV more negative than on copper and nickel, respectively, at -1.577 V vs. Hg/HgO (**Fig. 1a**).

With the exception of tin, all the graphite composite materials demonstrate significantly more negative  $E_{HER}$  values than the metallic substrates, as shown in **Fig. 1b**. The TF6, FR10 and PV15 substrates have  $E_{HER}$  values of -1.501, -1.532 and -1.550 V vs. Hg/HgO, respectively, which are more negative than that of copper or nickel. However, the corresponding Tafel slopes are lower, at 121 mV dec<sup>-1</sup> on TF6, 126 mV dec<sup>-1</sup> on FR10 and 133 mV dec<sup>-1</sup> on PV15. The BMA5 substrate provides the most negative  $E_{HER}$  of all, at -1.595 V vs. Hg/HgO, the Tafel slope is at 216 mV dec<sup>-1</sup>, a similar observation of the value of 208 mV dec<sup>-1</sup> was reported by Zheng *et al.* [51]. Despite the more negative hydrogen evolution onset potentials of the graphite composite materials, the rate of HER varies more strongly with overpotential at  $E < E_{HER}$ , compared to the metallic substrates. The hydrogen binding energy on graphite has been shown to be highly dependent on crystallographic orientation and adsorption location [52,53]. Of the materials tested here, the TF6, FR10 and PV15 substrates consist predominantly of graphite in the (00 $\bar{4}$ ) and (00 $\bar{6}$ ) basal planes, as shown in **Fig. S1** of the supplementary data, while the BMA substrate shows additional peaks in the ( $\bar{1}00$ ), ( $\bar{1}0\bar{1}$ ), ( $\bar{1}03$ ), ( $\bar{2}10$ ) and ( $\bar{2}1\bar{2}$ ) planes. Previously, it has been shown that hydrogen binding energy is significantly higher on non-basal planes [52] and this is believed to be the cause of the lower activity for HER on BMA5, compared to the other graphite composite substrates. The relatively small differences between the TF6, FR10 and PV15 materials are due to their differing polymer contents and conductivities (**Table 1**).

As shown in **Table 2** the zinc reduction onset potentials on each substrate ( $E_R$ ) are taken from the results of cyclic voltammetry in **Fig. 2** and the HER onset potentials ( $E_{HER}$ ) are taken from the results of LSV in **Fig. 1**. The  $E_{HER} - E_R$  values represent the difference between HER onset potential and zinc reduction potential on a given substrate and are used as an indicator of the likely HER contribution during zinc deposition. Clearly, increasingly negative  $E_{HER} - E_R$  values represent larger differences

between the HER and zinc reduction potentials and are favourable to the suppression of hydrogen evolution during zinc deposition. The positive values of  $E_{HER} - E_R$  on copper and nickel indicate that HER may commence at more positive potentials than zinc reduction on these substrates, resulting in significant HER occurring during zinc deposition. In all other cases  $E_{HER} - E_R$  is negative, with the largest differences occurring on BMA5 and tin, at -209 and -216 mV. These also display the highest Tafel slopes of 216 and 252 mV dec<sup>-1</sup>, respectively. In terms of hydrogen evolution suppression, this makes tin and BMA5 the most promising materials for use as zinc electrode substrates.

### 3.1.2 Cyclic voltammetry

Cyclic voltammetry has been carried out between -0.8 and -1.6 V vs. Hg/HgO, and the resultant voltammograms are given in **Fig. 2**. In all cases the cathodic peaks at around -1.44 V vs. Hg/HgO and anodic peaks at -1.24 V vs. Hg/HgO are due to bulk zinc reduction and oxidation, respectively. **Fig. 2b** displays a clear shoulder on the anodic peak and this appears to be caused by a secondary anodic peak at -1.08 V vs. Hg/HgO. This is indicative of the presence of zinc-copper alloying, with similar peaks in previous reports being attributed to zinc-copper alloy dissolution [3,31]. A similar shoulder is observed in the case of nickel (**Fig. 2a**) which may imply zinc-nickel alloying, although this has not previously been reported despite widespread use of nickel substrates for the alkaline zinc electrode [2,6,42]. No additional anodic peaks are observed for nickel (**Fig. 2a**) or copper substrates (**Fig. 2b**), indicating that these materials are stable within the applied potential range. Oxidation peaks for these metals have previously been observed by Wei *et al.* by extending the positive limit of cyclic voltammetry to 0.2 V vs. Hg/HgO [29].

For tin (**Fig. 2c**), an additional anodic response is observed commencing at -1.04 V vs. Hg/HgO with a peak at -0.854 V vs. Hg/HgO, and the corresponding cathodic peak at -1.03 V vs. Hg/HgO due to the oxidation and reduction of tin. This is in agreement with the previously reported voltammogram of Wei *et al.* [29]. Due to the presence of this reaction, the tin substrate may be prone to oxidation during zinc electrode cycling. While the zinc reduction peak is clear on tin (**Fig. 2c**), it is not well defined on nickel or copper (**Fig. 2a-b**) due to the onset of HER during zinc deposition, with further increases in cathodic current observed at increasingly negative potentials.

For the graphite composite substrates the voltammograms are very similar, as shown in **Fig. 2d**. In each case a nucleation loop is observed due to the additional overpotential required on the cathodic scan to form stable zinc nuclei on foreign substrates, such as graphite. For the deposition of zinc on metallic substrates no discernible nucleation overpotential is required, thus no nucleation loops are observed in **Fig. 2a-c**. The magnitude of zinc nucleation overpotential on each of the graphite composite materials is around 23 mV, as reflected by the zinc reduction onset potentials of between -1.382 and -1.384 V vs. Hg/HgO for these substrates, compared to -1.358 to -1.361 V vs. Hg/HgO on the metallic substrates, as shown in **Table 2**.

Anodic to cathodic charge ratios,  $Q_a / Q_c$ , for the voltammograms in **Fig. 2** are displayed in **Table 2** as a preliminary indicator of the coulombic efficiency of the zinc oxidation / reduction process on each substrate. For both the metallic and graphite composite materials, there is a clear increase in charge ratio as  $E_{HER} - E_R$  becomes more negative and the contribution of HER decreases. For the graphite composite substrates,  $Q_a / Q_c$  improves with increasingly negative  $E_{HER} - E_R$  in the order TF6 (0.845) → FR10 (0.871) → PV15 (0.878) → BMA5 (0.911), while for the metallic substrates  $Q_a / Q_c$  increases in the order; nickel (0.860) → copper (0.908) → tin (1.409). In the case of tin, the charge ratio exceeds unity due to the contribution of tin oxidation and reduction

(*Fig. 2c*). The result indicates that the most suitable substrates in terms of anodic to cathodic charge ratios are copper and BMA5 while tin is excluded for use as a zinc electrode substrate.

### 3.1.3 Zinc half-cell cycling

Example potential responses of the zinc electrode during half-cell cycling are provided in *Fig. 3*. For all seven substrates investigated, *Table 2* includes the mean coulombic efficiency, the mean zinc reduction ( $Z_{NR}$ ) and oxidation ( $Z_{NO}$ ) potentials, plus the ratio of  $Z_{NO}$  to  $Z_{NR}$  as an indicator of the potential effect of substrate material on full cell voltaic efficiency. While the potential responses are visually similar, initial potential spikes can be seen for the graphite composite substrates (*Fig. 3*) due to the nucleation overpotential of zinc on carbon. This is not observed for the metallic substrates, as expected from the results of cyclic voltammetry. The effect of nucleation overpotentials on mean zinc reduction potentials is not significant, as indicated by the fact that both  $Z_{NR}$  and  $Z_{NO}$  only differ by 15 mV (*Table 2*). As a result, the  $Z_{NO}/Z_{NR}$  values also show little variation, being 0.903 for copper and nickel, 0.912 for tin, and 0.919 for PV15 and BMA5.

The results of cyclic voltammetry indicate that tin oxidation commences at -1.04 V vs. Hg/HgO (*Fig. 2c*) and this may therefore occur during zinc electrode cycling to a cut off potential of -1.0 V vs. Hg/HgO. However, *Fig. 3* provides no evidence of a secondary oxidation plateau during cycling on the tin substrate or any clear augmentation of coulombic efficiency as a result of the oxidation of tin. The tin substrate therefore appears to be stable during these experiments. In this test, it has not been observed secondary discharge plateaus attributable to the dissolution of zinc alloys which previously had been observed for zinc-copper alloying by Bae [32]. But in that

case the charged zinc electrodes were aged to facilitate alloy formation. It is possible that extended cycling in this test may cause gradual alloying of zinc with the substrates and produce similar results. We will examine this in the future work.

The effect of substrate material on coulombic efficiency is clearer. For the metallic substrates, the coulombic efficiency increases from 91.5 % on nickel to 92.4 % on copper and 96.1 % on tin. This is in agreement with the results of Wei *et al.* who observed the same trend in coulombic efficiency for these three substrates during zinc deposition / dissolution cycling on a rotational disc electrode [29]. In the case of graphite composite substrates, the coulombic efficiency increases from 94.4 % on TF6 to 94.7 % on FR10, 95.9 % on PV15 and 96.7 % on BMA5. For all the substrate materials studied, the trend in coulombic efficiency directly relates to the trend in  $E_{HER}$  observed during linear sweep voltammetry and the  $E_{HER}-E_R$  values reported in **Table 2**. Substrates demonstrating increasingly negative  $E_{HER}$  and  $E_{HER}-E_R$  result in higher coulombic efficiencies in the order; nickel → copper → TF6 → FR10 → PV15 → tin → BMA5. Based on these results the BMA5 substrate is selected for zinc-nickel flow cell cycling tests as this displays the highest HER overpotential and zinc electrode coulombic efficiency (**Table 2**).

## 3.2 Zinc-nickel flow cell cycling

### 3.2.1 Effect of electrolyte flow rate

**Coulombic efficiency** - coulombic efficiencies per cycle obtained from galvanostatic cycling of a zinc nickel flow cell with electrolyte linear velocities of 1 to 12 cm s<sup>-1</sup> are provided in **Fig. 4a**. In many cases the performance of the cell rapidly becomes erratic, demonstrating poor and fluctuating coulombic efficiencies. **This behaviour was reported in our previous work [11,43], the low coulombic efficiency**

during the initial cycles is due to the limited discharge capacity of the nickel electrode.

When this occurs, the cell is allowed to continue cycling in order to obtain zinc depositions for subsequent characterisation and report the average coulombic efficiencies over a consistent number of cycles (*Table 3*). However, in order to maintain clarity, only a limited number of cycles are reported in *Fig. 4a*. This demonstrates that at an electrolyte velocity of  $1 \text{ cm s}^{-1}$  no stable charge-discharge cycles are achieved, the average coulombic efficiency resulting from continued cycling being just 91.7 %. At  $3 \text{ cm s}^{-1}$ , the coulombic efficiency improves to 93.0 % and a few stable cycles are observed before becoming erratic. At an average linear velocity of  $5 \text{ cm s}^{-1}$  stable performance over 80 charge / discharge cycles is achieved, with a significantly improved coulombic efficiency of 97.8 %. This is incrementally increased at an electrolyte velocity of  $7 \text{ cm s}^{-1}$  with the highest coulombic efficiency of 98.2 % obtained over 80 stable cycles. The trend for improved coulombic efficiency with increasing flow rates is due to enhanced zinc electrode discharge capacities (*Fig. 4b*) and can be directly related to the modification of zinc morphology, as discussed in section 3.2.2.

At linear electrolyte velocities of  $10$  and  $12 \text{ cm s}^{-1}$  coulombic efficiency once again diminishes, being around 94 % in both cases. *Fig. 4a* shows that performance in these cases is not erratic, but rather low in the early stages with a gradual improvement towards the level achieved at  $7 \text{ cm s}^{-1}$ . *Fig. 5a* displays this trend in coulombic efficiency with flow rate and demonstrates that this also applies when no electrolyte additive is present. The coulombic efficiencies are consistently lower in the case of no additive, however, indicating the benefit of the addition of 15 mM TEAH electrolyte additive previously reported [11,43].

*Fig. 4b* illustrates that the discharge behaviour of both zinc and nickel electrodes at the 50<sup>th</sup> cycle at all of the six flow rates. In all the cases, the cell was charged at  $20 \text{ mA cm}^{-2}$  to 3 mA h capacity and discharged at  $-20 \text{ mA cm}^{-2}$  to a cut off potential of 0.8

V. It can be seen that, at the lower flow rates (e.g.  $1 \text{ cm s}^{-1}$ ,  $3 \text{ cm s}^{-1}$ , and  $5 \text{ cm s}^{-1}$ ), the decrease of coulombic efficiency were cause by the zinc electrode indicating no sufficient deposited zinc to match the discharge capacity of nickel electrode. On the other hand, at the higher flow rates (e.g.  $7 \text{ cm s}^{-1}$ ,  $10 \text{ cm s}^{-1}$ , and  $12 \text{ cm s}^{-1}$ ), the discharge capacity becomes entirely limited by the nickel electrode. In this experiment, the coulombic efficiency has reached a maximum at  $7 \text{ cm s}^{-1}$  velocity due to a further improvement in the performance of the zinc electrode. At 10 and  $12 \text{ cm s}^{-1}$ , the discharge capacity of the nickel electrode continues to diminish, this consistently being the limiting factor to coulombic efficiency.

Thus, the improvement in coulombic efficiency at electrolyte velocities up to  $7 \text{ cm s}^{-1}$  is due to increased zinc electrode discharge capacities while the subsequent decrease in coulombic efficiency at higher flow rates is caused by degradation of nickel electrode discharge capacities. This behaviour presented here has not been reported by previous literature and we will continue to examine into detail of the effect of flow rates on both electrode behaviours.

***Voltaic and energy efficiencies*** – ***Fig. 5a*** indicates that the result of the polarisation effect of additive adsorption is a decrease in voltaic efficiencies with 15 mM TEAH. This largely offsets the improvement in coulombic efficiency provided by the additive. It also demonstrates small increases in voltaic efficiencies with electrolyte velocities up to  $7 \text{ cm s}^{-1}$  both with no additive and with 15 mM TEAH. This is due predominantly to a reduction in zinc electrode charge / discharge polarisation ( $Z_{no} - Z_{NR}$ ) with increasing flow rates, as shown in ***Fig. 5b***, decreased by 35 and 29 mV in the case of no additive and 15 mM TEAH, respectively. As shown in ***Table 3***, the nickel electrode polarisation remains relatively consistent, changing by less than 15 mV across the whole range of flow rates employed. The decrease in  $Z_{no} - Z_{NR}$  along with increasing flow rates is associated with improved mass transport of zincate species. This

reduces concentration polarisation and electrode overpotentials, resulting in improved voltaic efficiencies.

The coulombic and voltaic efficiencies all peak at  $7 \text{ cm s}^{-1}$ , being 96.5 % and 90 % in the case of no additive and 98.2 % and 88.2 % with the addition of 15 mM TEAH. The resultant energy efficiencies are almost identical at around 87 %. This performance is similar to that of Cheng *et al.* [2]. However, they employed a lower current density of  $10 \text{ mA cm}^{-2}$  alongside a very high electrolyte velocity of  $19.5 \text{ cm s}^{-1}$ . Here, an electrolyte velocity of  $7 \text{ cm s}^{-1}$  achieves stable performance with a similar average energy efficiency, even at the higher current density of  $20 \text{ mA cm}^{-2}$ .

### 3.2.2 Characterisation of zinc morphology

**Fig. 6** shows SEM images of surface morphology of zinc electrodepositions obtained after 80 charge / discharge cycles in a zinc-nickel flow cell at varying flow rates. Under low magnification of 100, at lower flow rates of  $1 \text{ cm s}^{-1}$  and  $3 \text{ cm s}^{-1}$ , as shown in **Fig. 6a and 6b**, the zinc electrode surfaces were finished with boulder type deposits consisting of large spheroidal structures, while at higher flow rates of  $5\text{-}12 \text{ cm s}^{-1}$  (**Fig. 6c - 6f**) the electrode surfaces have kept in a mode of relatively smooth and compact deposit. If examining closely in **Fig. 6a and 6b**, these obvious boulder structures are appeared, leading to relatively low coulombic efficiency of 91.7 % at  $1 \text{ cm s}^{-1}$  and 93 % at  $3 \text{ cm s}^{-1}$ . It is assumed due to the reduced diffusion limitations to zinc deposition, evidenced by the attenuation of  $Z_{no} - Z_{nr}$  to 95 mV at the flow rate of  $3 \text{ cm s}^{-1}$  for example.

An electrolyte velocity of  $5 \text{ cm s}^{-1}$  clearly marks a transition, with the zinc morphology shown in **Fig. 6c** being largely smooth and compact. The corresponding zinc electrode polarisation is further reduced to 87 mV and flow cell cycling becomes

stable with a significantly improved coulombic efficiency of 97.8 %. At this point diffusion limitations to zinc reduction can be assumed to be minimal, with further increases to electrolyte velocity producing no significant change in concentration polarisation, as indicated by consistent  $Z_{NO} - Z_{NR}$  values (**Table 3**). **Fig. 6d** shows a smooth and compact deposition of zinc obtained at an electrolyte velocity of  $7 \text{ cm s}^{-1}$ , which is indicative of charge transfer limited zinc reduction [41], as demonstrated by the  $Z_{NO} - Z_{NR}$  value reaching a minimum of 85 mV. Coulombic efficiency in the flow cell reaches a peak value of 98.2 % at this electrolyte velocity. However, increased electrolyte velocities of 10 and  $12 \text{ cm s}^{-1}$  show no further improvement in zinc morphology, as shown in **Fig. 6e** and **Fig. 6f**, respectively, which are also reflected by decreased coulombic efficiencies of 94.2 % at  $10 \text{ cm s}^{-1}$  and 94.6 % at  $12 \text{ cm s}^{-1}$ . As discussed in section 3.2.1, this is caused by the capacity limitation at the nickel electrode.

XRD patterns of zinc deposit samples obtained at the end of 80 charge / discharge cycles under varying flow rates are given in **Fig. S2**. In all cases, the deposits consist of hexagonal closed packed (hcp) crystallites predominantly in the (101) plane at  $43.2^\circ$ , with a secondary peak at  $36.3^\circ$  in the (002) plane and tertiary (100) peaks at  $39.0^\circ$ . Further minor peaks are observed at  $70.1^\circ$ ,  $70.6^\circ$ ,  $77.1^\circ$ ,  $82.1^\circ$  and  $86.6^\circ$  relating to the (103), (210), (004), (212) and (201) planes respectively. The small peaks at  $42.3^\circ$  and  $44.5^\circ$  are due to the presence of hcp graphite in the (100) and (101) planes, caused by the graphite / PVDF electrode substrate. Across the range of flow rates, there is no significant variation in the relative magnitude of zinc peaks, indicating that the orientation of crystallites within the zinc deposits remains quite unaffected by flow rate. However, the crystallite size, estimated by Scherrer's equation with a shape factor of 0.9 (**Table S1**), is reduced from 78 nm at  $1 \text{ cm s}^{-1}$  to 37 nm at  $7 \text{ cm s}^{-1}$ , before increasing a little at higher electrolyte velocities, being 58 nm at  $12 \text{ cm s}^{-1}$ . This refinement of

crystallite size with increasing flow rates is due to a larger number of nucleation sites occurring as mass transport of  $\text{Zn(OH)}_4^{2-}$  to the electrode improves, an effect previously observed by Youssef *et al.* [54].

This is elucidated by **Fig. 6a**, which shows areas at which little zinc deposition has occurred in an electrolyte flowing at  $1 \text{ cm s}^{-1}$ . At  $3 \text{ cm s}^{-1}$ , while the zinc morphology remains bulbous, the distribution of these structures on the electrode is more consistent, indicating an increased number of nucleation sites (**Fig. 6b**). This results in a refinement of grain size from 78 to 62 nm. Once zinc reduction occurs under predominantly charge transfer controlled conditions, at velocities of  $5 \text{ cm s}^{-1}$  and above, the active species are readily available and nucleation takes place at a larger number of evenly distributed locations, resulting in the smooth zinc morphologies observed in **Fig. 6c-d**. Subsequently, crystallite size is further reduced to 43 nm at  $5 \text{ cm s}^{-1}$  and 37 nm at  $7 \text{ cm s}^{-1}$ .

### 3.2.3 Current density ratio and zinc morphology

The ratio of applied current density to limiting current density  $j / j_{lim}$  has previously been proposed as an indicator of zinc morphology [55,56]. The limiting current density,  $j_{lim}$ , in the flow cell employed here may be found by equation (2) [55,57]:

$$j_{lim} = \frac{nFD C_o Sh}{d_e} \quad (2)$$

Where  $n$  is the number of electrons involved in the reaction,  $F$  is Faradays constant,  $C_o$  is the concentration of  $\text{Zn(OH)}_4^{2-}$  in  $\text{mol L}^{-1}$ ,  $d_e$  is the hydraulic diameter of the cell,  $D$  is the diffusion coefficient of  $\text{Zn(OH)}_4^{2-}$  and  $Sh$  is the Sherwood number in the cell, found by equation (3) [55,57]:

$$Sh = 1.85 \left( \frac{ReScd_e}{L} \right)^{1/3} \quad (3)$$

Where  $L$  is the length of the electrode in the streamwise direction and  $Sc$  is the Schmidt number. A diffusion coefficient of  $2.25 \times 10^{-6} \text{ cm}^2 \text{ s}^{-1}$  has been employed, as determined through RDE experimentation reported in our previous work [43].

**Table 4** displays the resultant values of  $j_{lim}$  and  $j/j_{lim}$ , along with mean coulombic efficiencies for the range of zinc-nickel flow cell cycling tests completed. Values of  $j/j_{lim} \geq 1$  signify diffusion limited zinc reduction and can be expected to result in dendritic morphologies. Boulder type morphologies can be expected at  $j/j_{lim}$  values close to but less than 1 due to mixed control conditions. At some lower value of  $j/j_{lim}$ , a transition from mixed control to charge transfer control should then occur, resulting in compact zinc depositions. By relating the  $j/j_{lim}$  values at  $20 \text{ mA cm}^{-2}$  (**Table 4**) to the zinc morphologies shown in **Fig. 6** this transition can be observed.

The boulder type morphologies in **Fig. 6a-b** are a result of  $j/j_{lim} \geq 0.47$ , while the compact zinc depositions in **Fig. 6c-f** are obtained with  $j/j_{lim} \leq 0.39$ . The transition from mixed to charge transfer controlled zinc reduction can therefore be concluded to occur in the region of  $0.47 > j/j_{lim} > 0.39$ . The region of  $1 > j/j_{lim} > 0.39$  represents an area of diminishing diffusion limitations with increasing flow rates and  $j_{lim}$  values resulting in decreasing  $j/j_{lim}$  ratios. The improvement in coulombic efficiencies during flow cell cycling observed across this range, both at  $20$  and  $50 \text{ mA cm}^{-2}$  (**Table 4**) seem to support this, with decreasing  $j/j_{lim}$  ratios resulting in increases to coulombic efficiency. This can be assumed to be due to the improving quality of zinc depositions with reduced diffusion limitations discussed in section 3.2.2.

At  $80 \text{ mA cm}^{-2}$   $j/j_{lim}$  is consistently in excess of 1, signifying that zinc reduction occurs under diffusion limited conditions at all flow rates employed. Dendritic zinc morphologies are therefore expected to occur, as previously shown by Banerjee *et al.*

[56]. Variation of  $j/j_{lim}$  at values over 1 may be expected to be inconsequential to zinc morphology, with zinc reduction being diffusion limited in any case. Coulombic efficiency at  $80 \text{ mA cm}^{-2}$  decreases with increasing  $j/j_{lim}$ , however, from 82.5 % at  $j/j_{lim} = 1.17$  to 78.3 % at  $j/j_{lim} = 1.25$  and 78.7 % at  $j/j_{lim} = 1.40$ . This is attributed to the occurrence of parasitic HER, as the applied current exceeds the limiting current for zinc reduction at  $j/j_{lim} > 1$ . The transport of  $\text{Zn}(\text{OH})_4^{2-}$  to the electrode is therefore inadequate to facilitate sufficient zinc reduction, resulting in increasing contributions from HER as  $j/j_{lim}$  increases.

The result indicates that  $j/j_{lim}$  values of 0.39 or less result in compact zinc depositions due to charge transfer limited zinc reduction. Values of  $j/j_{lim}$  between 0.39 and 1 yield boulder type morphologies under mixed control conditions, decreasing in quality as  $j/j_{lim}$  increases. While not observed, it is assumed that dendritic zinc will occur at  $j_{lim} \geq 1$  under purely diffusion limited control. This is in general agreement with the work of many previous researchers [7,8,36–38,56].

### **3.2.4 Zinc-nickel flow cell stability testing**

In order to validate the cell performance reported in section 3.2.1, the zinc-nickel flow cell has been operated over an extended number of charge / discharge cycles applying the best performing parameters previously identified. The graphite / PVDF composite (BMA5) selected in section 3.1 is employed as the zinc electrode substrate material, and an electrolyte velocity of  $7 \text{ cm s}^{-1}$  selected following the results in section 3.2.1. A current density of  $20 \text{ mA cm}^{-2}$  and a 15 mM concentration of TEAH additive is utilised in a 6 M KOH / 0.5 M ZnO electrolyte, this being identified as a promising addition to the electrolyte in our previous work [11,43].

In this case, 200 charge / discharge cycles were completed using the conditions outlined above prior to the data reported here. This is to minimise the effect of the development of nickel electrode performance observed in preceding results and may be considered as a conditioning phase for the zinc-nickel flow cell. **Fig. 7a** reports the obtained efficiencies per cycle. Example charge / discharge curves [at both zinc and nickel electrodes](#) are provided in **Fig. 7b**, demonstrating highly consistent electrode performance over 200 charge / discharge cycles.

The average coulombic, voltaic and energy efficiencies are 98.3, 88.1 and 86.6 %, respectively. This performance represents only a small improvement to that achieved by Cheng *et al.* [2]. However, the current density applied here is 20 mA cm<sup>-2</sup> compared to 10 mA cm<sup>-2</sup> in that work. In addition, the electrolyte velocity of 7 cm s<sup>-1</sup> employed here is 64 % lower than the 19.5 cm s<sup>-1</sup> employed by Cheng *et al.* This improvement is due to two factors. Firstly, the employment of the BMA5 graphite / PVDF zinc electrode substrate material reduces the contribution of parasitic HER during zinc reduction. Secondly, the inclusion of TEAH facilitates favourable zinc morphologies at reduced electrolyte flow rates.

## 4. Conclusions

Three metallic and four graphite composite materials as zinc electrode substrates have been assessed in terms of their hydrogen evolution overpotentials and effect on coulombic efficiency of the zinc electrode. It is found that the charge / discharge coulombic efficiency of the zinc electrode increases as hydrogen evolution onset potentials become more negative in the order: nickel → copper → TF6 → FR10 → PV15 → tin → BMA5. The BMA5 graphite / PVDF composite substrate demonstrates

the highest coulombic efficiency at 96.7 % and most negative hydrogen evolution onset potential at -1.595 V vs. Hg/HgO.

Utilising the BMA5 graphite composite as a zinc electrode substrate, electrolyte velocities from 1 to 12 cm s<sup>-1</sup> have been applied to the zinc-nickel flow cell and the effect on cell performance and zinc morphology studied. Zinc morphology undergoes a transition from spongy boulder like structures under mixed control zinc reduction at electrolyte velocities under 5 cm s<sup>-1</sup> to smooth and compact morphologies under charge transfer control at higher velocities. This transition is related to the ratio of applied current density to limiting current density  $j/j_{lim}$ . At current density ratios between 0.47 and 1 boulder type zinc morphologies have been shown to occur, while smooth and compact zinc depositions are obtained at current density ratios of 0.39 and below. Current density ratio may be used to inform design and operation of alkaline zinc electrode flow batteries, ensuring that zinc reduction occurs under charge transfer limited conditions to achieve stable and highly efficient performance.

The best performance during galvanostatic cycling is achieved at a current density of 20 mA cm<sup>-2</sup> with an electrolyte velocity of 7 cm s<sup>-1</sup> and 15 mM TEAH as an electrolyte additive. Coulombic, voltaic and energy efficiencies over 80 stable charge / discharge cycles are 98.2, 88.2, and 86.7%, respectively. The same conditions are applied over a larger number of cycles, with an average energy efficiency of nearly 87 % achieved over 200 cycles with virtually no sign of degradation.

## **Acknowledgements**

The authors would like to acknowledge the support received from C-Tech Innovation Ltd (John Collins and David Hall), WhEST Ltd (Ian Whyte), and SGL carbon (Kathlyne Duong). Funding: This work was supported by the Engineering and

Physical Sciences Research Council (EPSRC) Supergen Energy Storage Project (grant number: EP/P003494/1) entitled 'Zinc-Nickel Redox Flow Battery for Energy Storage'; the EPSRC PhD studentship as a Doctoral Training Partnership (DTP); and the support from the College of Engineering, Mathematics and Physical Sciences in the University of Exeter.

## References

- [1] P. Leung, X. Li, C. Ponce De León, L. Berlouis, C.T.J. Low, F.C. Walsh, Progress in redox flow batteries, remaining challenges and their applications in energy storage, *RSC Adv.* 2 (2012) 10125–10156. <https://doi.org/10.1039/c2ra21342g>.
- [2] J. Cheng, L. Zhang, Y.-S. Yang, Y.-H. Wen, G.-P. Cao, X.-D. Wang, Preliminary study of single flow zinc–nickel battery, *Electrochem. Commun.* 9 (2007) 2639–2642. <https://doi.org/10.1016/j.elecom.2007.08.016>.
- [3] L. Zhang, J. Cheng, Y. Yang, Y. Wen, X. Wang, G. Cao, Study of zinc electrodes for single flow zinc/nickel battery application, *J. Power Sources.* 179 (2008) 381–387. <https://doi.org/10.1016/j.jpowsour.2007.12.088>.
- [4] Y. Ito, M. Nyce, R. Plivelich, M. Klein, D. Steingart, S. Banerjee, Zinc morphology in zinc-nickel flow assisted batteries and impact on performance, *J. Power Sources.* 196 (2011) 2340–2345. <https://doi.org/10.1016/j.jpowsour.2010.09.065>.
- [5] Y. Cheng, Q. Lai, X. Li, X. Xi, Q. Zheng, C. Ding, H. Zhang, Zinc-nickel single flow batteries with improved cycling stability by eliminating zinc accumulation on the negative electrode, *Electrochim. Acta.* 145 (2014) 109–115. <https://doi.org/10.1016/j.electacta.2014.08.090>.
- [6] Y. Cheng, H. Zhang, Q. Lai, X. Li, D. Shi, L. Zhang, A high power density single flow zinc–nickel battery with three-dimensional porous negative electrode, *J. Power Sources.* 241 (2013) 196–202. <https://doi.org/10.1016/j.jpowsour.2013.04.121>.
- [7] J.O. Bockris, Z. Nagy, A. Damjanovic, On the Deposition and Dissolution of Zinc in Alkaline Solutions, *J. Electrochem. Soc.* 119 (1972) 285. <https://doi.org/10.1149/1.2404188>.
- [8] R.Y. Wang, D.W. Kirk, G.X. Zhang, Effects of Deposition Conditions on the Morphology of Zinc Deposits from Alkaline Zincate Solutions, *J. Electrochem. Soc.* 153 (2006) C357. <https://doi.org/10.1149/1.2186037>.
- [9] B. Sharifi, M. Mojtahedi, M. Goodarzi, J. Vahdati Khaki, Effect of alkaline electrolysis conditions on current efficiency and morphology of zinc powder, *Hydrometallurgy.* 99 (2009) 72–76. <https://doi.org/10.1016/j.hydromet.2009.07.003>.
- [10] V. Ravindran, V.S. Muralidharan, Cathodic processes on zinc in alkaline zincate solutions, *J. Power Sources.* 55 (1995) 237–241. [https://doi.org/10.1016/0378-7753\(95\)02184-I](https://doi.org/10.1016/0378-7753(95)02184-I).
- [11] D.P. Trudgeon, K. Qiu, X. Li, T. Mallick, O.O. Taiwo, B. Chakrabarti, V. Yufit, N.P. Brandon, D. Crevillen-Garcia, A. Shah, Screening of effective electrolyte additives for zinc-based redox flow battery systems, *J. Power Sources.* 412 (2019) 44–54. <https://doi.org/10.1016/j.jpowsour.2018.11.030>
- [12] K. Bass, P.J. Mitchell, G.D. Wilcox, J. Smith, Methods for the reduction of shape

- change and dendritic growth in zinc-based secondary cells, *J. Power Sources*. 35 (1991) 333–351. [https://doi.org/10.1016/0378-7753\(91\)80117-G](https://doi.org/10.1016/0378-7753(91)80117-G).
- [13] Y. Wen, J. Cheng, L. Zhang, X. Yan, Y. Yang, The inhibition of the spongy electrocrystallization of zinc from doped flowing alkaline zincate solutions, *J. Power Sources*. 193 (2009) 890–894. <https://doi.org/10.1016/j.jpowsour.2009.04.047>.
- [14] I.N. Justinijanović, J.N. Jovičević, A.R. Despić, The effect of foreign atoms on the properties of electrolytic zinc powders, *J. Appl. Electrochem.* 3 (1973) 193–200. <https://doi.org/10.1007/BF00619161>.
- [15] Y.F. Yuan, J.P. Tu, H.M. Wu, S.F. Wang, W.K. Zhang, H. Huang, Effects of stannous ions on the electrochemical performance of the alkaline zinc electrode, *J. Appl. Electrochem.* 37 (2007) 249–253. <https://doi.org/10.1007/s10800-006-9249-1>.
- [16] T. Kakeya, A. Nakata, H. Arai, Z. Ogumi, Enhanced zinc electrode rechargeability in alkaline electrolytes containing hydrophilic organic materials with positive electrode compatibility, *J. Power Sources*. 407 (2018) 180–184. <https://doi.org/10.1016/j.jpowsour.2018.08.026>.
- [17] J.C. Ballesteros, P. Diaz-Arista, Y. Meas, R. Ortega, G. Trejo, Zinc electrodeposition in the presence of polyethylene glycol 20000, *Electrochim. Acta.* 52 (2007) 3686–3696. <https://doi.org/10.1016/j.electacta.2006.10.042>.
- [18] S.J. Banik, R. Akolkar, Suppressing Dendritic Growth during Alkaline Zinc Electrodeposition using Polyethylenimine Additive, *Electrochim. Acta.* 179 (2015) 475–481. <https://doi.org/10.1016/j.electacta.2014.12.100>.
- [19] S.J. Banik, R. Akolkar, Suppressing Dendrite Growth during Zinc Electrodeposition by PEG-200 Additive, *J. Electrochem. Soc.* 160 (2013) D519–D523. <https://doi.org/10.1149/2.040311jes>.
- [20] M. Liang, H. Zhou, Q. Huang, S. Hu, W. Li, Synergistic effect of polyethylene glycol 600 and polysorbate 20 on corrosion inhibition of zinc anode in alkaline batteries, *J. Appl. Electrochem.* 41 (2011) 991–997. <https://doi.org/10.1007/s10800-011-0328-6>.
- [21] J.L. Ortiz-Aparicio, Y. Meas, T.W. Chapman, G. Trejo, R. Ortega, E. Chainet, Electrodeposition of zinc in the presence of quaternary ammonium compounds from alkaline chloride bath, *J. Appl. Electrochem.* 45 (2015) 67–78. <https://doi.org/10.1007/s10800-014-0777-9>.
- [22] C.J. Lan, C.Y. Lee, T.S. Chin, Tetra-alkyl ammonium hydroxides as inhibitors of Zn dendrite in Zn-based secondary batteries, *Electrochim. Acta.* 52 (2007) 5407–5416. <https://doi.org/10.1016/j.electacta.2007.02.063>.
- [23] G.D. Wilcox, P.J. Mitchell, Electrolyte additives for zinc-anoded secondary cells II. Quaternary ammonium compounds, *J. Power Sources*. 32 (1990) 31–41. [https://doi.org/10.1016/0378-7753\(90\)80031-8](https://doi.org/10.1016/0378-7753(90)80031-8).
- [24] J. Zhu, Y. Zhou, C. Gao, Influence of surfactants on electrochemical behavior of

- zinc electrodes in alkaline solution, *J. Power Sources*. 72 (1998) 231–235.  
[https://doi.org/10.1016/S0378-7753\(97\)02705-5](https://doi.org/10.1016/S0378-7753(97)02705-5).
- [25] A. Gomes, M.I.S. Pereira, Zn electrodeposition in the presence of surfactants Part I. Voltammetric and structural studies, *Electrochim. Acta*. 52 (2006) 863–871.  
<https://doi.org/10.1016/j.electacta.2006.06.025>.
- [26] Y. Wen, T. Wang, J. Cheng, J. Pan, G. Cao, Y. Yang, Lead ion and tetrabutylammonium bromide as inhibitors of the growth of spongy zinc in single flow zinc/nickel batteries, *Electrochim. Acta*. 59 (2012) 64–68.  
<https://doi.org/10.1016/j.electacta.2011.10.042>.
- [27] Y. Cheng, H. Zhang, Q. Lai, X. Li, Q. Zheng, X. Xi, C. Ding, Effect of temperature on the performances and in situ polarization analysis of zinc–nickel single flow batteries, *J. Power Sources*. 249 (2014) 435–439.  
<https://doi.org/10.1016/j.jpowsour.2013.10.115>.
- [28] G. Adzic, J. McBreen, M.G. Chu, Adsorption and Alloy Formation of Zinc Layers on Silver, *J. Electrochem. Soc.* 128 (1981) 1691–1697.  
<https://doi.org/10.1149/1.2127712>.
- [29] X. Wei, D. Desai, G.G. Yadav, D.E. Turney, A. Couzis, Impact of anode substrates on electrodeposited zinc over cycling in zinc-anode rechargeable alkaline batteries, *Electrochim. Acta*. 212 (2016) 603–613.  
<https://doi.org/10.1016/j.electacta.2016.07.041>.
- [30] J. McBreen, M.G. Chu, G. Adzic, Substrate Effects on Zinc Deposition from Zincate Solutions: II. Deposition on Pb, Tl, Sn and In, *J. Electrochem. Soc.* 128 (1981) 2287–2292. <https://doi.org/10.1149/1.2127236>.
- [31] M.G. Chu, J. McBreen, G. Adzic, Substrate Effects on Zinc Deposition from Zincate Solutions: I. Deposition on Cu, Au, Cd and Zn, *J. Electrochem. Soc.* 128 (1981) 2281–2286.
- [32] I.T. Bae, Alloy Formation at Electrodeposited Zinc–Copper Electrode Interfaces at Room Temperature, *J. Electrochem. Soc.* 155 (2008) D395.  
<https://doi.org/10.1149/1.2891134>.
- [33] J. McBreen, E. Gannon, D.T. Chin, R. Sethi, Zinc Electrode Morphology in Alkaline Solutions: II. Study of Alternating Charging Current Modulation on Pasted Zinc Battery Electrodes, 130 (1983) 1641–1645.
- [34] G. Nikiforidis, L. Berlouis, D. Hall, D. Hodgson, Evaluation of carbon composite materials for the negative electrode in the zinc-cerium redox flow cell, *J. Power Sources*. 206 (2012) 497–503. <https://doi.org/10.1016/j.jpowsour.2011.01.036>.
- [35] G. Nikiforidis, L. Berlouis, D. Hall, D. Hodgson, A study of different carbon composite materials for the negative half-cell reaction of the zinc cerium hybrid redox flow cell, *Electrochim. Acta*. 113 (2013) 412–423.  
<https://doi.org/10.1016/j.electacta.2013.09.061>.
- [36] R.D. Naybour, The Effect of Electrolyte Flow on the Morphology of Zinc Electrodeposited from Aqueous Alkaline Solution Containing Zincate Ions, *J.*

- Electrochem. Soc. 116 (1969) 520–524. <https://doi.org/10.1149/1.2411939>.
- [37] A.R. Despic, J. Diggle, J.O. Bockris, Mechanism of the Formation of Zinc Dendrites, *J. Electrochem. Soc.* 115 (1968) 507–508. <https://doi.org/10.1149/1.2411297>.
- [38] J.W. Diggle, A.R. Despic, J.O. Bockris, The Mechanism of the Dendritic Electrocrystallization of Zinc, *J. Electrochem. Soc.* 116 (1969) 1503–1514. <https://doi.org/10.1149/1.2411588>.
- [39] K. Wang, P. Pei, Z. Ma, H. Xu, P. Li, X. Wang, Morphology control of zinc regeneration for zinc–air fuel cell and battery, *J. Power Sources.* 271 (2014) 65–75. <https://doi.org/10.1016/j.jpowsour.2014.07.182>.
- [40] Y. Ito, M. Nyce, R. Plivelich, M. Klein, S. Banerjee, Gas evolution in a flow-assisted zinc–nickel oxide battery, *J. Power Sources.* 196 (2011) 6583–6587. <https://doi.org/10.1016/j.jpowsour.2011.03.025>.
- [41] Y. Cheng, X. Xi, D. Li, X. Li, Q. Lai, H. Zhang, Performance and potential problems of high power density zinc-nickel single flow batteries, *RSC Adv.* 5 (2015) 1772–1776. <https://doi.org/10.1039/c4ra12812e>.
- [42] Y. Cheng, H. Zhang, Q. Lai, X. Li, D. Shi, Performance gains in single flow zinc–nickel batteries through novel cell configuration, *Electrochim. Acta.* 105 (2013) 618–621. <https://doi.org/10.1016/j.electacta.2013.05.024>.
- [43] D.P. Trudgeon, X. Li, The effect of electrolyte and additive concentration on zinc–nickel flow cell performance, *Electrochim. Acta.* (2020). <https://doi.org/10.1016/j.electacta.2020.137479>.
- [44] A. Bard, R. Parson, J. Jordan, *Standard Potentials in Aqueous Solution*, 1st ed., Marcel Dekker Inc., New York, 1985.
- [45] W. Sheng, M. Myint, J.G. Chen, Y. Yan, Correlating the hydrogen evolution reaction activity in alkaline electrolytes with the hydrogen binding energy on monometallic surfaces, *Energy Environ. Sci.* 6 (2013) 1509–1512. <https://doi.org/10.1039/c3ee00045a>.
- [46] S. Trasatti, Work function, electronegativity, and electrochemical behaviour of metals. III. Electrolytic hydrogen evolution in acid solutions, *J. Electroanal. Chem.* 39 (1972) 163–184. [https://doi.org/10.1016/S0022-0728\(72\)80485-6](https://doi.org/10.1016/S0022-0728(72)80485-6).
- [47] M.F. Kibria, M.S. Mridha, A.H. Khan, Electrochemical studies of a nickel electrode for the hydrogen evolution reaction, *Int. J. Hydrogen Energy.* 20 (1995) 435–440. [https://doi.org/10.1016/0360-3199\(94\)00073-9](https://doi.org/10.1016/0360-3199(94)00073-9).
- [48] M. Gong, D.Y. Wang, C.C. Chen, B.J. Hwang, H. Dai, A mini review on nickel-based electrocatalysts for alkaline hydrogen evolution reaction, *Nano Res.* 9 (2016) 28–46. <https://doi.org/10.1007/s12274-015-0965-x>.
- [49] P. Ferrin, S. Kandoi, A.U. Nilekar, M. Mavrikakis, Hydrogen adsorption, absorption and diffusion on and in transition metal surfaces: A DFT study, *Surf. Sci.* 606 (2012) 679–689. <https://doi.org/10.1016/j.susc.2011.12.017>.

- [50] J.K. Nørskov, T. Bligaard, A. Logadottir, J.R. Kitchin, J.G. Chen, S. Pandalov, U. Stimming, Trends in the Exchange Current for Hydrogen Evolution, *J. Electrochem. Soc.* 152 (2005) J23. <https://doi.org/10.1149/1.1856988>.
- [51] Y. Zheng, Y. Jiao, L.H. Li, T. Xing, Y. Chen, M. Jaroniec, S.Z. Qiao, Toward design of synergistically active carbon-based catalysts for electrocatalytic hydrogen evolution, *ACS Nano*. 8 (2014) 5290–5296. <https://doi.org/10.1021/nn501434a>.
- [52] F.H. Yang, R.T. Yang, Ab initio molecular orbital study of adsorption of atomic hydrogen on graphite: Insight into hydrogen storage in carbon nanotubes, *Carbon N. Y.* 40 (2002) 437–444. [https://doi.org/10.1016/S0008-6223\(01\)00199-3](https://doi.org/10.1016/S0008-6223(01)00199-3).
- [53] S. Letardi, M. Celino, F. Cleri, V. Rosato, Atomic hydrogen adsorption on a Stone-Wales defect in graphite, *Surf. Sci.* 496 (2002) 33–38. [https://doi.org/10.1016/S0039-6028\(01\)01437-6](https://doi.org/10.1016/S0039-6028(01)01437-6).
- [54] K.M. Youssef, C.C. Koch, P.S. Fedkiw, Influence of pulse plating parameters on the synthesis and preferred orientation of nanocrystalline zinc from zinc sulfate electrolytes, *Electrochim. Acta.* 54 (2008) 677–683. <https://doi.org/10.1016/j.electacta.2008.07.048>.
- [55] Y. Ito, X. Wei, D. Desai, D. Steingart, S. Banerjee, An indicator of zinc morphology transition in flowing alkaline electrolyte, *J. Power Sources.* 211 (2012) 119–128. <https://doi.org/10.1016/j.jpowsour.2012.03.056>.
- [56] D. Desai, X. Wei, D.A. Steingart, S. Banerjee, Electrodeposition of preferentially oriented zinc for flow-assisted alkaline batteries, *J. Power Sources.* 256 (2014) 145–152. <https://doi.org/10.1016/j.jpowsour.2014.01.026>.
- [57] J. Newman, E. Thomas-Alyea, Karen, *Electrochemical Systems*, 3rd ed., John Wiley & Sons Inc., New York, 2004.
- [58] W.M. Haynes, D.R. Lide, T.J. Bruno, *Handbook of Chemistry and Physics*, 97th ed., CRC Press, London, 2017.

*Table 1: Zinc electrode substrate materials under investigation.*

<b>Material</b>	<b>Supplier</b>	<b>Conductivity / S cm<sup>-1</sup></b>	<b>Details</b>
BMA5 Graphite / PVDF composite	Eisenhuth	$1.6 \times 10^2$	5 % PVDF content
PV15 Graphite / fluoropolymer composite	SGL Carbon	$1.7 \times 10^2$	15 % polymer content
TF6 Graphite / fluoropolymer composite	SGL Carbon	$1.3 \times 10^2$	6 % polymer content
FR10 Graphite / thermoset resin composite	SGL Carbon	$2.9 \times 10^2$	10 % polymer content
Copper foil	Goodfellow	$6.0 \times 10^5$ [58]	99.99 % purity, 0.5 mm thickness
Tin foil	Goodfellow	$9.7 \times 10^4$ [58]	99.99 % purity, 0.5 mm thickness
Nickel foil	Goodfellow	$1.44 \times 10^5$ [58]	99.99 % purity, 0.5 mm thickness

**Table 2:** Results of linear sweep voltammetry, cyclic voltammetry and zinc half-cell cycling. Data taken from Figures 1 to 3.

Substrate	HER onset potential, $E_{HER}$ / V vs. Hg/HgO	Zinc reduction onset potential, $E_R$ / V vs. Hg/HgO	$E_{HER} - E_R$ / mV	Anodic/cathodic charge ratio, $Q_a/Q_c$ , -0.8 to -1.6 / V vs. Hg/HgO	Mean reduction potential, $Zn_R$ / V vs. Hg/HgO	Mean oxidation potential, $Zn_O$ / V vs. Hg/HgO	$Zn_O / Zn_R$	Average coulombic efficiency / %
Nickel	-1.126	-1.360	234	0.860	-1.429	-1.290	0.903	91.5
Copper	-1.332	-1.358	26	0.908	-1.429	-1.291	0.903	92.4
Tin	-1.577	-1.361	-216	1.409	-1.418	-1.293	0.912	96.1
TF6	-1.501	-1.383	-118	0.845	-1.424	-1.290	0.906	94.4
FR10	-1.532	-1.382	-150	0.871	-1.416	-1.300	0.918	94.7
PV15	-1.550	-1.382	-168	0.878	-1.414	-1.299	0.919	95.9
BMA5	-1.595	-1.384	-209	0.911	-1.414	-1.299	0.919	96.7

**Table 3:** Average zinc electrode potentials, coulombic, voltaic and energy efficiencies over 80 charge / discharge cycles in an electrolyte solution of 6 M KOH + 0.5 M ZnO with and without addition of 15 mM TEAH at varying electrolyte flow rates.

Electrolyte linear velocity, $u$ / $\text{cm s}^{-1}$	Mean zinc reduction potential, $Zn_R$ , vs. Hg/HgO / V	Mean zinc oxidation potential, $Zn_O$ , vs. Hg/HgO / V	Average zinc electrode polarisation, $Zn_O - Zn_R$ / mV	Coulombic efficiency / %	Voltaic efficiency / %	Energy efficiency / %
<b>No additive: -</b>						
1	-1.417	-1.342	75	87.7	89.2	78.2
3	-1.411	-1.354	57	90.0	89.8	80.8
5	-1.410	-1.360	50	95.2	89.6	85.2
7	-1.396	-1.356	40	96.5	90.0	86.8
10	-1.397	-1.359	38	93.4	90.5	84.5
12	-1.394	-1.355	39	93.3	90.5	84.4
<b>15 mM TEAH: -</b>						
1	-1.453	-1.339	114	91.7	87.1	79.9
3	-1.440	-1.345	95	93.0	87.3	81.2
5	-1.437	-1.350	87	97.8	87.9	86.0
7	-1.432	-1.347	85	98.2	88.2	86.7
10	-1.433	-1.346	87	94.2	88.1	83.0
12	-1.432	-1.345	87	94.6	88.0	83.2

**Table 4:** Limiting currents, current density ratios and mean coulombic efficiencies for the range of zinc-nickel flow cell cycling tests undertaken

Electrolyte linear velocity, $u$ / $\text{cm s}^{-1}$	Limiting current density, $j_{\text{lim}} / \text{mA cm}^{-2}$	20 $\text{mA cm}^{-2}$		50 $\text{mA cm}^{-2}$		80 $\text{mA cm}^{-2}$	
		$j / j_{\text{lim}}$	Mean coulombic efficiency / %	$j / j_{\text{lim}}$	Mean coulombic efficiency / %	$j / j_{\text{lim}}$	Mean coulombic efficiency / %
1	30	0.67	91.7	-	-	-	-
3	43	0.47	93.0	-	-	-	-
5	51	0.39	97.8	-	-	-	-
7	57	0.35	98.2	0.88	79.0	1.40	78.7
10	64	0.31	94.2	0.78	82.8	1.25	78.3
12	68	0.29	94.6	0.73	88.6	1.17	82.5

## Figure Captions

**Figure 1:** Polarisation curves of: (a) metallic substrates, (b) graphite composite substrates in 6 M KOH electrolyte solution. Working electrode area:  $0.25 \text{ cm}^2$ . Potential sweep rate:  $1 \text{ mV s}^{-1}$ . (c) Tafel plots of HER on substrate materials.

**Figure 2:** Cyclic voltammograms on various substrate materials in 6 M KOH + 0.5 M ZnO electrolyte solution: (a) nickel, (b) copper, (c) tin, (d) graphite composites. Working electrode area:  $0.25 \text{ cm}^2$ . Potential sweep rate:  $10 \text{ mV s}^{-1}$ .

**Figure 3:** Potential vs. time responses from zinc half-cell cycling in 6 M KOH + 0.5 M ZnO electrolyte solution on the substrates under investigation. Working electrode area:  $0.25 \text{ cm}^2$ . Zinc reduction conducted at  $-20 \text{ mA cm}^{-2}$  for 30 minutes, and oxidation at  $20 \text{ mA cm}^{-2}$  to a cut off potential of  $-1.0 \text{ V vs. Hg/HgO}$ .

**Figure 4:** Results of zinc-nickel flow cell cycling over 80 cycles in 6 M KOH + 0.5 M ZnO with 15 mM TEAH; (a) coulombic efficiency vs. cycle number, (b) electrode potentials during discharge of the 50th cycles. Cell charged at  $20 \text{ mA cm}^{-2}$  to 3 mA h capacity and discharged at  $-20 \text{ mA cm}^{-2}$  to a cut off potential of  $0.8 \text{ V}$ . Electrode areas:  $1 \text{ cm}^2$ .

**Figure 5:** Results of zinc-nickel flow cell cycling over 80 cycles in 6 M KOH + 0.5 M ZnO with no additive or 15 mM TEAH; (a) average efficiencies as a function of electrolyte flow rates, (b) Zinc electrode charge / discharge polarisation vs. electrolyte flow rate. Cell charged at  $20 \text{ mA cm}^{-2}$  to 3 mA h capacity and discharged at  $-20 \text{ mA cm}^{-2}$  to a cut off potential of  $0.8 \text{ V}$ . Electrode areas:  $1 \text{ cm}^2$ .

**Figure 6:** SEM images of zinc deposit morphologies obtained after 80 charge / discharge cycles in a zinc-nickel flow cell with electrolyte solutions containing 6 M KOH + 0.5 M ZnO + 15 mM TEAH at various electrolyte flow rates: (a)  $1 \text{ cm s}^{-1}$ , (b)  $3 \text{ cm s}^{-1}$ , (c)  $5 \text{ cm s}^{-1}$ , (d)  $7 \text{ cm s}^{-1}$ , (e)  $10 \text{ cm s}^{-1}$ , (f)  $12 \text{ cm s}^{-1}$ . SEM magnifications: 100 (inserts: 25 k). Accelerating voltage 5 kV. Working distance 5 mm.

**Figure 7:** (a) Efficiencies as a function of cycle number and (b) electrode charge / discharge potential curves in a zinc-nickel flow cell during 200 charge / discharge cycles in an electrolyte solution of 6 M KOH + 0.5 M ZnO + 15 mM TEAH at a flow rate of  $7 \text{ cm s}^{-1}$ . Cell charged at  $20 \text{ mA cm}^{-2}$  to 3 mA h capacity and discharged at  $-20 \text{ mA cm}^{-2}$  to a cut off potential of  $0.8 \text{ V}$ . Electrode areas:  $1 \text{ cm}^2$ .

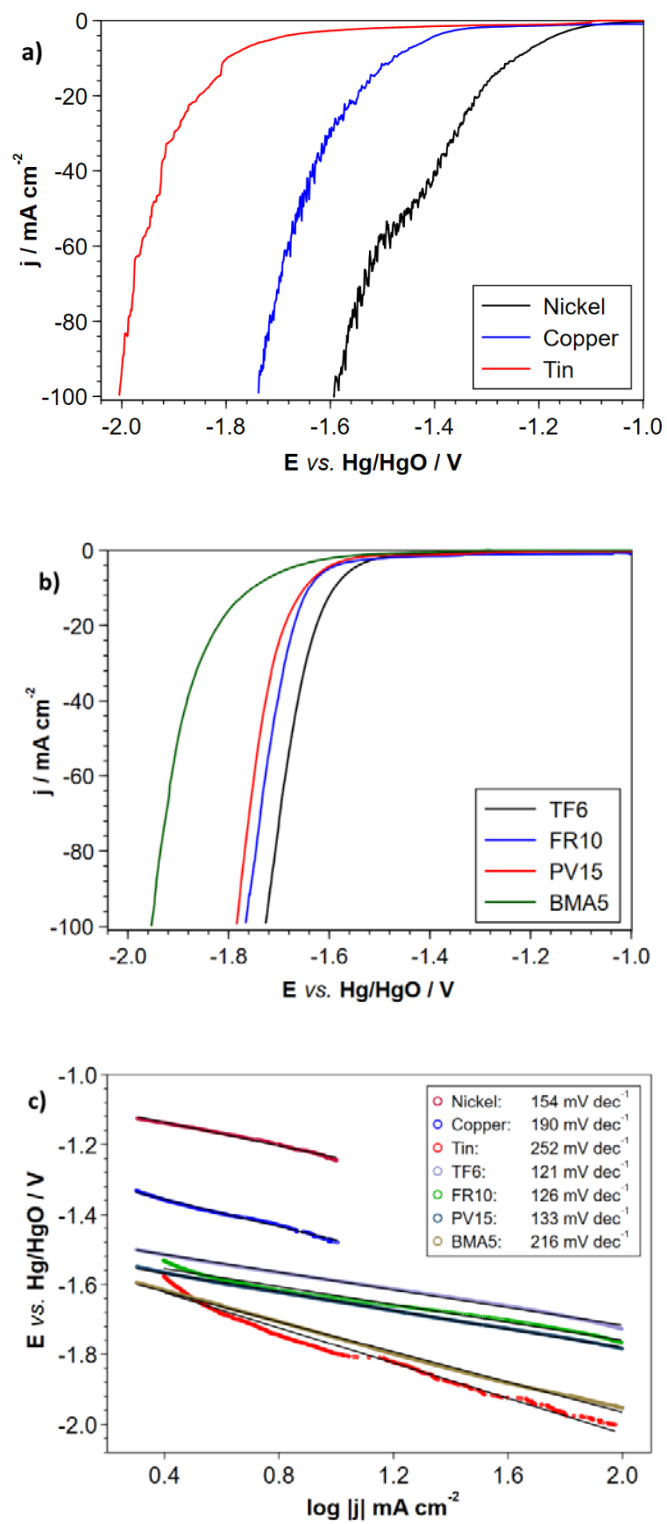


**Figure 2**

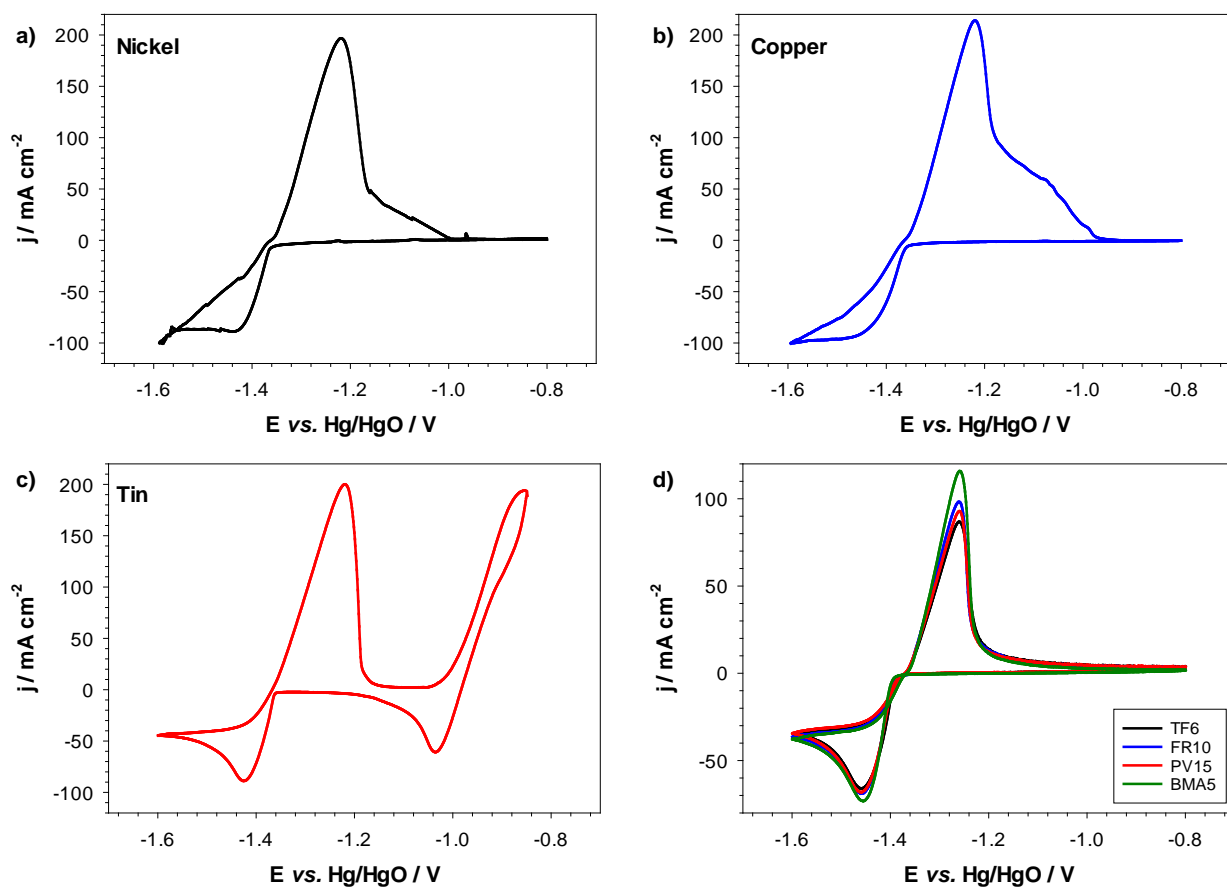


Figure 2

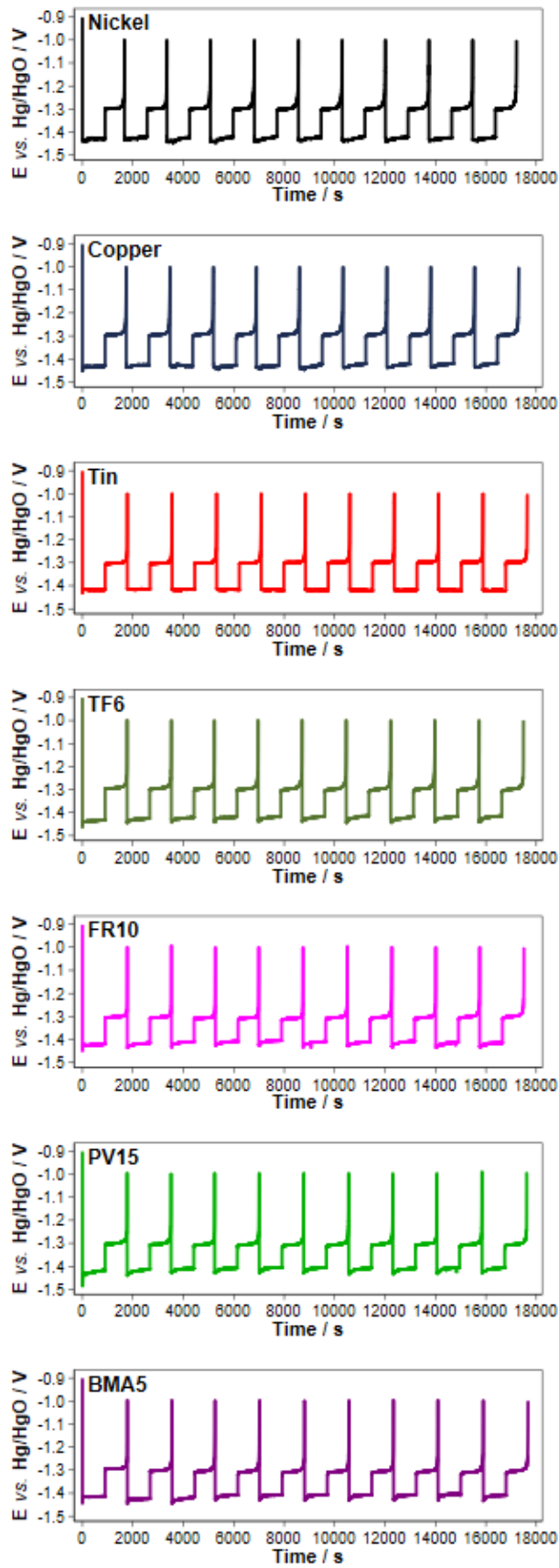
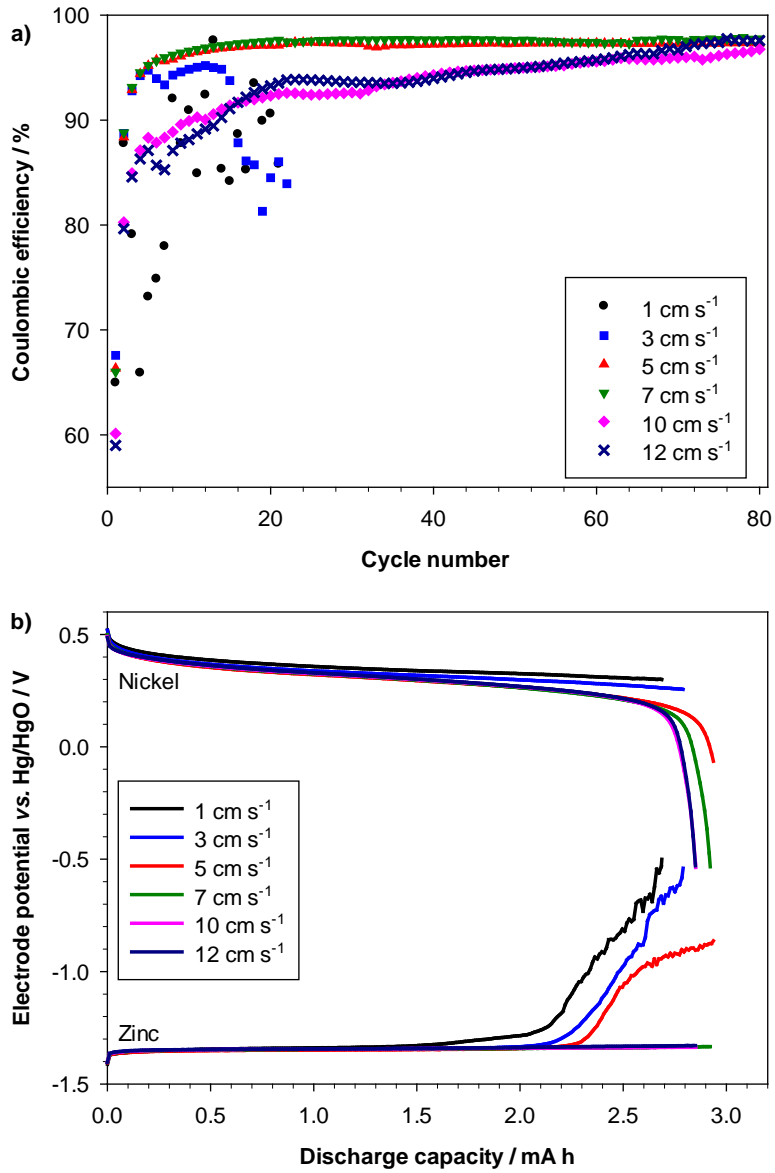
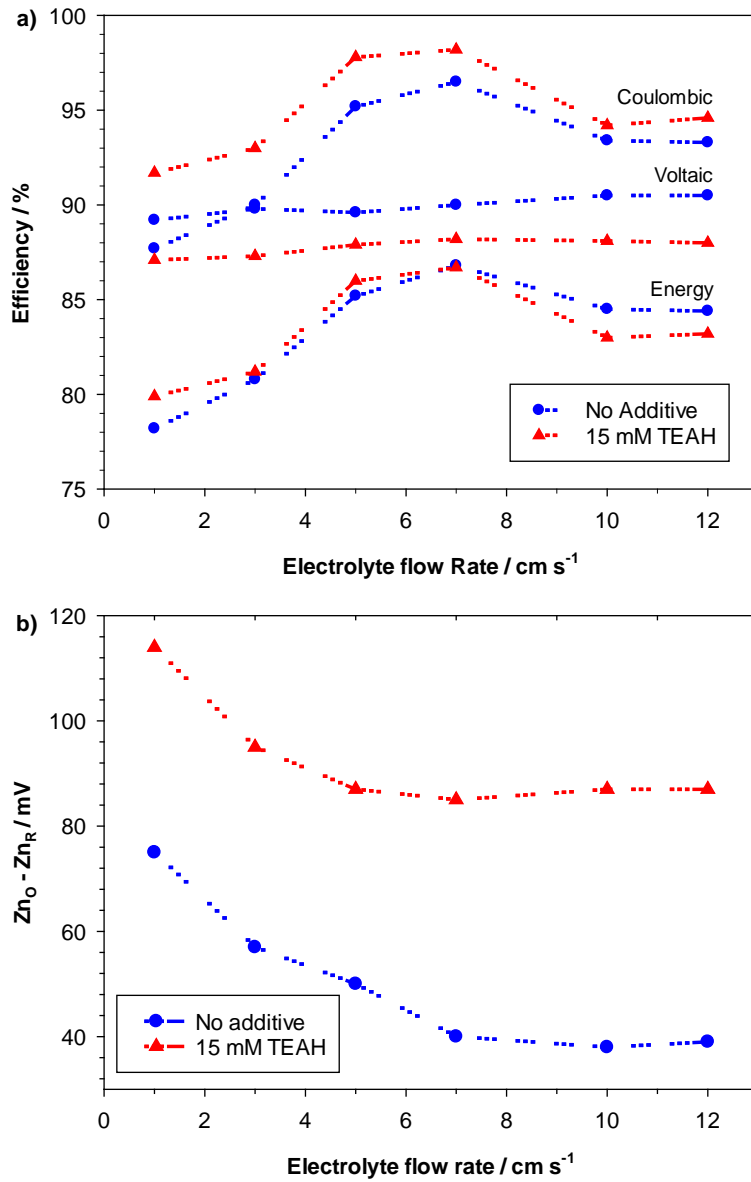


Figure 3



**Figure 4**



**Figure 5**

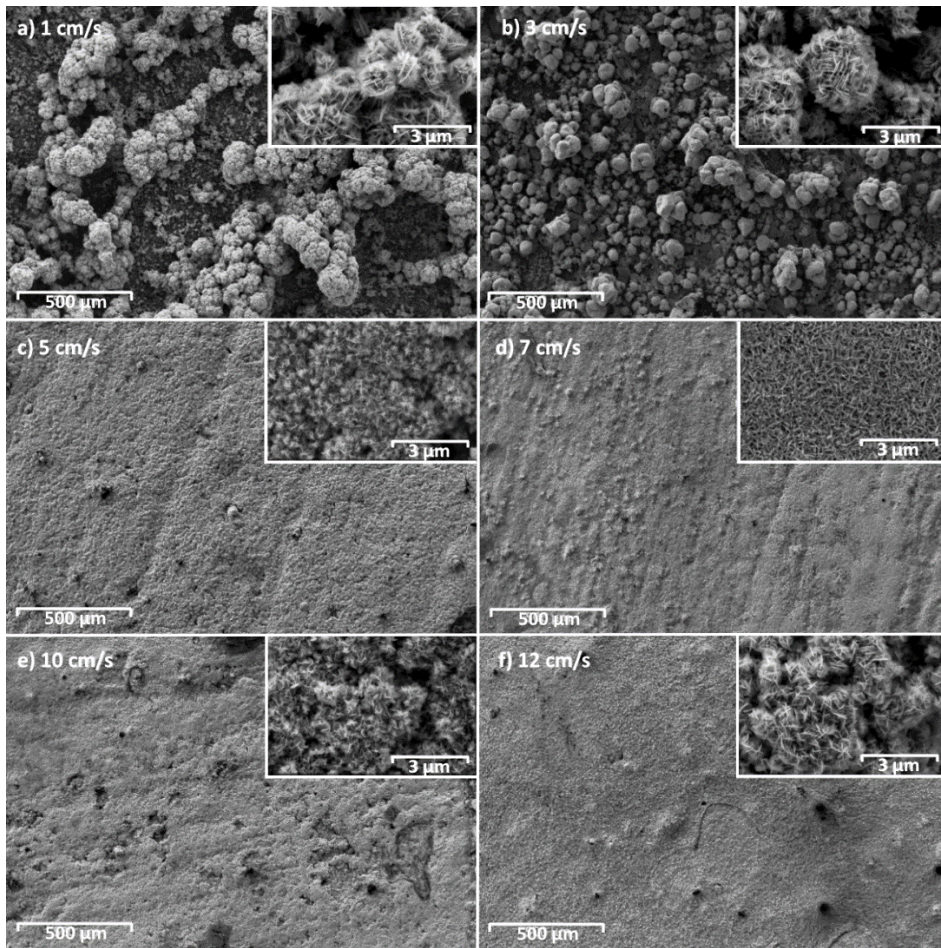


**Figure 6**

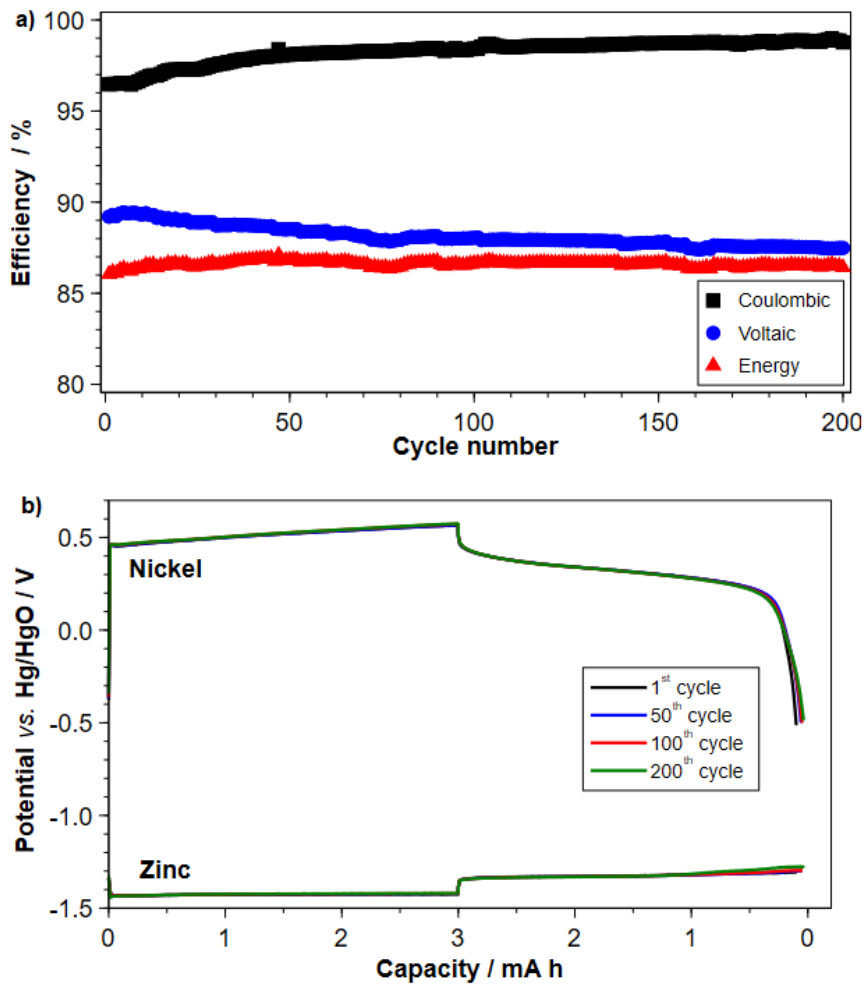


Figure 7